

Growth of Large Single-Crystalline Monolayer Hexagonal Boron Nitride by Oxide-Assisted Chemical Vapor Deposition

*Ren-Jie Chang,¹ Xiaochen Wang,¹ Shanshan Wang,¹ Yuewen Sheng,¹ Ben Porter,¹ Harish
Bhaskaran,¹ Jamie H. Warner^{1*}*

¹Department of Materials, University of Oxford, Parks Road, Oxford, OX1 3PH, United
Kingdom

*Jamie.Warner@materials.ox.ac.uk

Keywords h-BN, CVD, oxide passivation layer, 2D materials

Abstract

Hexagonal boron nitride (h-BN) films are considered as the ideal insulating substrate for other two-dimensional materials (2D) growth to construct heterostructure device due to its atomically smooth surface and lack of dangling bonds. Many efforts have been made on reducing the domain boundaries via controlling its nucleation density in the chemical vapor deposition (CVD) growth, but most of the domain size for h-BN crystal are still in the magnitude of several micrometers and the h-BN crystals are mostly random-orientated, making the h-BN films defective. Here, we modified the growth by introducing an oxide passivating layer on the Cu surface before the growth of h-BN. The nucleation density can be reduced from 10^6 mm^{-2} to 10^3 mm^{-2} and the nucleation domain size can be increased from $1 \text{ }\mu\text{m}$ to $20 \text{ }\mu\text{m}$. The h-BN domains within each Cu grain are well-orientated, indicating epitaxial relationship between the h-BN crystals and the Cu growth substrates and leads to larger crystal domains within the film

of $\sim 100\mu\text{m}$. This CVD approach removes the need for expensive Pt foil catalysts for large area continuous films of hBN monolayers.

Introduction

The enormous success of graphene research has sparked immense interest in the development of a wide range of complementary, atomically thin two-dimensional (2D) materials that possess unique structures and electronic properties. Two-dimensional hexagonal boron nitride (h-BN) is similar to graphene in its structure but with alternating B and N atoms arranged in its monolayer honeycomb structure, and is the thinnest insulating material with an electrical bandgap of 5.9 eV.¹ It poses not only superior mechanical flexibility, chemical and temperature stability but also high thermal conductivity.²⁻⁵ These fascinating properties make h-BN a good candidate for various applications such as a membranes for strong oxidation resistance, deep ultraviolet emitters, quantum photonic emitters, encapsulation layers and tunneling barriers in field effect tunneling transistors.⁶⁻¹⁰ In addition, h-BN is also considered as a promising insulating substrate for semi-metallic graphene and semiconducting metal dichalcogenides growth to construct a van der Waals (vdW) heterostructures for electronic and photovoltaic devices that exhibit unique characteristics and are unobtainable from single-component 2D materials.¹¹⁻¹⁴

All these extensive applications of h-BN requires high quality and uniformity. Elimination of defects and precise control of layer number are therefore highly demanded as it could directly affect the performance and physical properties of the devices. In comparison to traditional top-down exfoliation approaches,¹⁵⁻¹⁶ bottom-up vapor phase growth is scalable and compatible with many fabrication processes. The size of synthetic h-BN crystals grown by vapour phase can be larger than chemical exfoliation method.¹⁷ The area of the h-BN films is only determined by the area of the substrate. This method has been widely adopted to grow

large area h-BN films. The growth method has been reported on a range of transition catalyst metals (including Cu,¹⁸ Ni,¹⁹ Pt,²⁰⁻²¹ Fe,²² Co,²³ Ir,²⁴ Ru,²⁵ Rh²⁶ and Ag²⁷) and other insulating substrate such as SiO₂ and sapphire that allow the direct growth of other 2D materials on h-BN without any additional transfer process.²⁸⁻²⁹ The precursors used for h-BN growth range from gas (diborane and ammonia),³⁰ liquid (borazine)²¹ to solid (ammonia borane and trimethylamine borane).³¹⁻³² A variety of growth techniques to achieve atomically thin h-BN films over large distance have been obtained through chemical vapor deposition (CVD), physical vapor deposition (PVD) and molecular beam epitaxy (MBE).³³⁻³⁶ CVD is an attractive method for the growth of h-BN due to its low-cost, simplicity in design and operation. The domain size for h-BN to date, however, is still much smaller than that of graphene grown on commonly used Cu substrates. This is attributed to the much smaller adsorption energies of the B-N pair in h-BN crystal on the Cu surface compared to that of a pair of graphene carbon atoms on the basis of density function theory (DFT) calculations.³⁷⁻³⁸ The nucleation of h-BN on Cu can consequently be achieved with much lower surface supersaturations of precursors. The domain sizes of CVD grown h-BN were typically in the orders of micrometer.

Similar to the improvement of graphene films quality, several works have been accomplished to control the nucleation density and increase the domain size by electrochemical polishing,³⁹ melting and re-solidifying of the Cu substrates.⁴⁰⁻⁴¹ Other common strategies including controlling the amount of precursors,⁴² annealing time and flowrate of catalytic hydrogen gas,⁴³ changing the growth substrate into Cu-Ni alloy or Fe are also beneficial for the enhancement of h-BN domain size.⁴⁴⁻⁴⁵ More recently, it was shown that the presence of oxygen on Cu surface can greatly reduce the density of graphene nuclei by several orders of magnitude.⁴⁶⁻⁴⁹ However, such a chemical growth route has not been applied to h-BN yet. Here, we study the growth of highly-crystalline monolayer h-BN through introducing a thin oxide layer on Cu substrate prior to the growth stage. This CVD approach assisted by the pre-formed

oxide layer, denoted as OCVD, exhibits a reduction of h-BN nucleation density at the initial growth stage and can reach a continuous film when increasing the growth time. The highly aligned orientation of triangular h-BN domains over large-area indicates the epitaxial relationship between h-BN and Cu substrate. The as-grown h-BN monolayers were also characterized by using Raman spectroscopy, atomic force microscopy, scanning electron microscopy and transmission electron microscopy.

Results and discussion

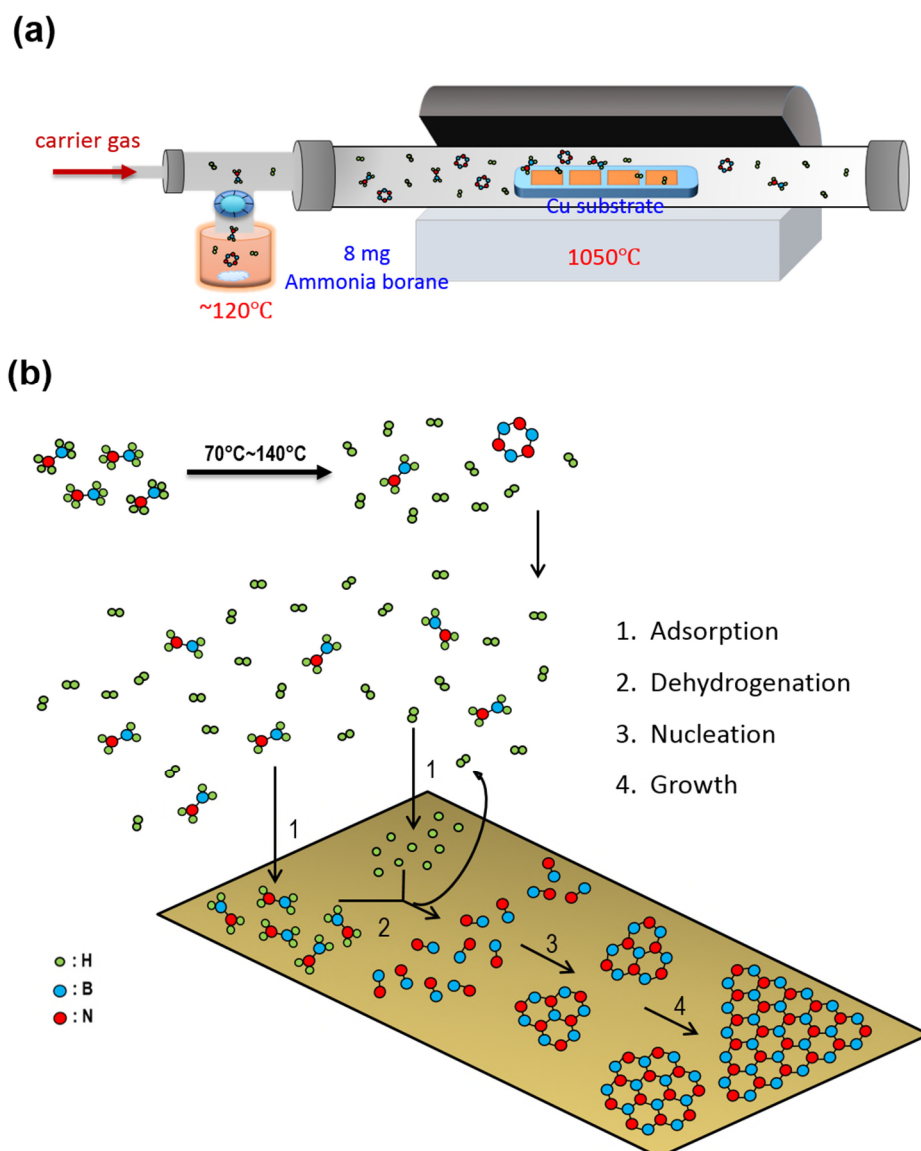


Figure 1. Atmospheric pressure CVD synthesis of h-BN on copper. (a) Schematic illustration of the mechanisms in the growth of graphene on Cu surface by chemical vapor deposition. (b) Schematic illustration of the CVD experimental set-up with polished copper foils in a ceramic crucible.

Figure 1(a) schematically shows the experiment setup for the CVD growth of h-BN with the Cu catalytic substrate placing on the ceramic crucible. The synthesis of monolayer h-BN was carried out using a custom built 1-inch CVD system with quartz tube and gas flow rates controlled by digital mass flow controllers. Ammonia borane (BH_3NH_3) powder was used

as h-BN growth source and placed into a small chamber with the heating belt in the upstream of the CVD furnace. The two separated heating system provides better temperature control, and the amount of the feedstocks can be controlled by the needle valve between the small chamber and the quartz tube. Prior to h-BN growth, the ammonia borane powder was heated up to 120°C with the needle valve closed. The growth of h-BN commences when the needle valve is open, allowing the precursors to diffuse to Cu substrate surface at high temperature regime.

The elementary surface processes involved in the CVD growth of monolayer h-BN on Cu substrate is schematically shown in Figure 1(b). Firstly, ammonia borane used as a precursor is thermally decomposed in the temperature ranging from 70°C to 140°C. The decomposition of ammonia borane produces gaseous hydrogen, borazine and aminoborane. These gaseous molecules are adsorbed on the Cu surface when carried to the Cu substrate by argon gas. Secondly, the adsorbed hydrogen atoms dehydrogenate the aminoborane molecules and generate active species such as BN dimers which are contributive to the h-BN growth. Because these active species are thermally unstable, they tend to agglomerate to form a stable h-BN nuclei when its supersaturation is high enough. Here, the surface irregularities such as grain boundaries and the rough surface of Cu are known to stimulate the h-BN nucleation. Thirdly, the rest of the active species attach to the existing h-BN nuclei and enlarge the domain through surface diffusion that is driven by a concentration gradient. Finally, the continual supply of active species give rise to the coalescence of adjacent h-BN domains into a continuous film when the h-BN domains is growing large enough. It is also noted that in our experiments, the CVD growth is conducted under the ambient pressure, so that the evaporation of Cu atoms resulted from the high growth temperature (1050°C), which is close to the melting point of Cu (1083°C), is less impactful to the h-BN growth compared with the low-pressure CVD growth.

The surface roughness of Cu substrate plays a critical role in reducing the nucleation density of h-BN crystals. Figure S1 demonstrates the effect of substrate polishing on the h-BN nucleation density. Due to the rolling process from the fabrication of Cu foils, the as-purchased Cu substrate contain surface parallel textures. The h-BN domains tend to nucleate along these textures because of the existence of dense surface irregularities and dangling bonds from substrate around these textures (Figure S1(a-c)). In comparison, the h-BN domains grown on mechanical polished Cu substrates shows a suppression of nucleation density (Figure S1(d-f)) because of the smoothened surface. The lower nucleation density on polished Cu substrates also reveals decreasing surface coverage under the same growth condition. This allows the production of h-BN crystals with larger domain size and higher quality.

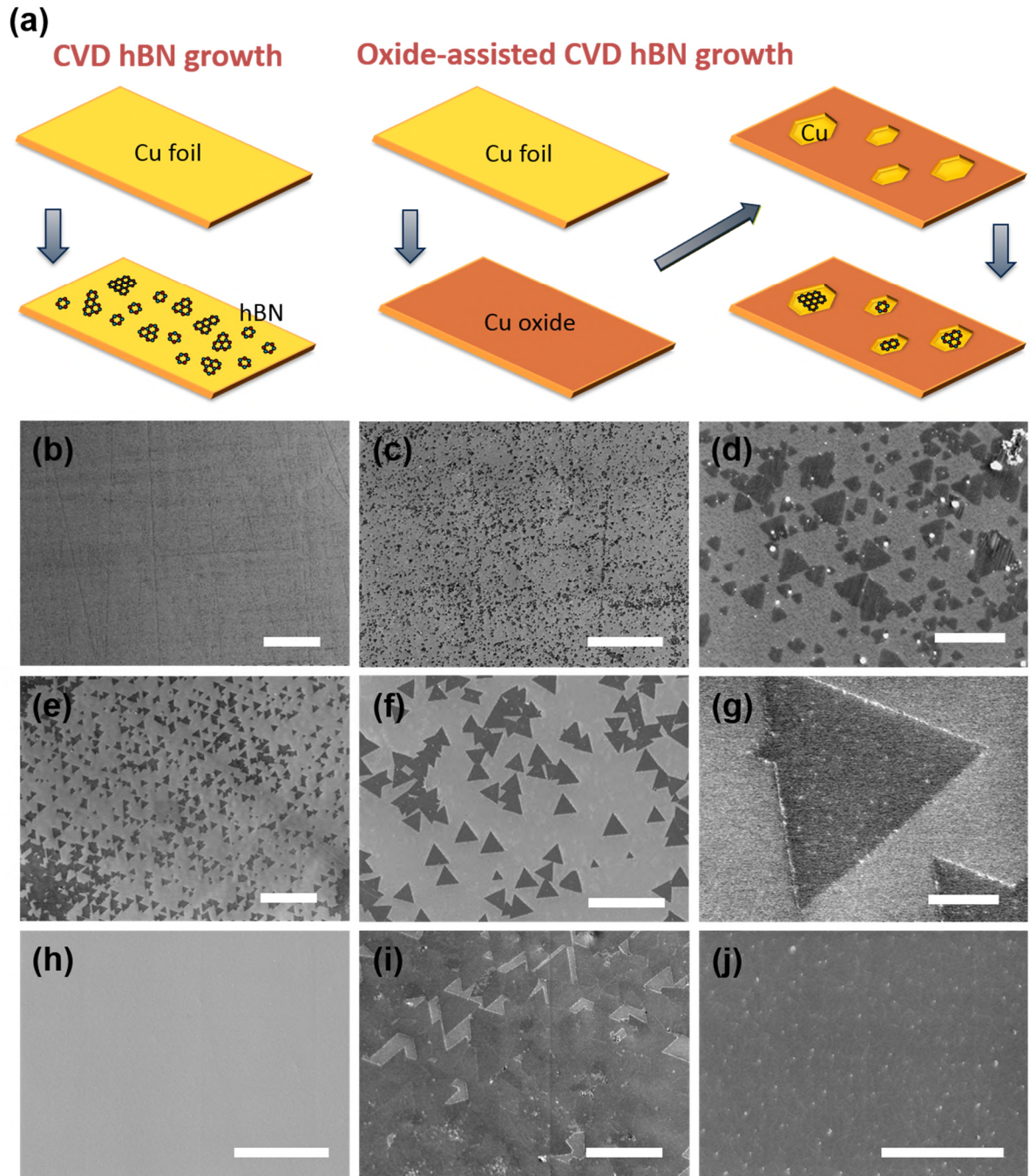


Figure 2 OCVD growth of large h-BN domains on Cu substrate from sporadic to continuous film.

(a) Schematic illustrations showing the h-BN growth mechanism by conventional CVD process and OCVD process with pre-formed oxide layer on Cu substrates. (b-d) SEM image of h-BN grown for 10 min in the conventional CVD process. (e-g) SEM image of h-BN grown for 30 min in the OCVD process. (h-j) SEM images of h-BN grown by OCVD process in 10, 45 and 60 minutes, respectively. The scale bar is 100 μm in (b) and (e), 30 μm in (c), (f), (h-j) and 5 μm in (d) and (g).

Figure 2(a) schematically explains the growth mechanism in reducing the initial nucleation density of h-BN through the OCVD growth. In conventional CVD growth process the active species are generated from the decomposition of ammonia borane precursor, leading to boron and nitrogen-containing species nucleating and forming small domains. Because the Cu surface contains dense surface irregularities including surface steps, dislocation threads, and impurities that could be the preferred nucleation sites, h-BN nucleates randomly on the Cu surface at the initial growth stage, the domain boundaries inevitably exist when coarsening of the domains and eventually forming into a continuous h-BN film. By contrast, in the OCVD growth process the Cu substrate is firstly oxidized forming a thin oxide layer on the surface. Because the boron and nitrogen-containing species have higher binding energy to nucleate on the oxide layer, the pre-formed oxide layer passivates the nucleation sites of Cu surfaces before h-BN growth. In the following h-BN growth stage the oxide layer gradually decomposes in the reducing hydrogen atmosphere and only the limited fresh Cu surface is able to absorb the active species and form a stable nuclei. This allows the subsequent active species absorbed on the Cu substrate tend to attach the initial h-BN nuclei by surface diffusion, so that the number of preferred nucleation sites is reduced.

The suppression of nucleation density due to the surface oxide passivating layer is shown in the SEM images in Figure 2(b-g). The nucleation density could be reduced from 10^6 mm^{-2} to 10^3 mm^{-2} . As a result, the h-BN domains grown in the conventional CVD process are randomly nucleated on Cu surface ranging from $0.5 \text{ }\mu\text{m}$ to $5 \text{ }\mu\text{m}$ (Figure 2(b-d)), while the h-BN domain size grown in the OCVD process is about $20 \text{ }\mu\text{m}$ (Figure 2(e-g)). Because h-BN nucleation only occurs after the passivating Cu oxide layer is decomposed, the growth of h-BN is slower in the OCVD process. In conventional CVD process it takes about 10 minutes of growth time to reach 50% surface coverage for h-BN domains (Figure 2(b-d)), but in the OCVD process no distinct h-BN domains are observed within the 10 min growth (Figure 2(h)). The h-

BN growth proceeds when increasing the growth time to 45 min (Figure 2(i)), and the monolayer h-BN growth is almost completed by 60 min growth (Figure 2(j)). It is also noted that several white particles and wrinkles are usually observed in the h-BN surface. The white particles might be associated with the stable byproducts such as borazine decomposed from the ammonium borane precursors, and the wrinkles are attributed to the negative thermal expansion coefficient of h-BN, resulting the shrinkage of h-BN but expansion of the underlying Cu substrate during the cooling stage.

The comparison between heating profiles for the furnace as a function of time and the gas flow rate used for growing h-BN during each timeline in conventional CVD and OCVD process are demonstrated in Figure S2. In the conventional CVD process, the whole system was first flushed with argon gas and then ramped up to a high temperature in a reducing atmosphere. The copper was annealed for at least one hour after the furnace reached the desired growth temperature. The growth of h-BN was then proceeded on Cu by introducing the decomposed ammonia borane precursors. By contrast, because the oxide layer is prone to decompose at high temperature, the annealing was cancelled and hydrogen was turned off before the growth stage to stabilize the oxide layer on Cu surface in the OCVD h-BN growth process.

The OCVD-grown h-BN also exhibited different morphology in different Cu substrates. Figure S3 shows the different domain shape of h-BN obtained from each Cu substrate in our OCVD setup and is attributed to the misbalance between B and N atoms. Although ammonia borane precursor has equimolar stoichiometry (B/N ratio = 1:1), it is reported that the edge with N-termination is energetic favorable than that with B-termination,⁵⁰ resulting in a triangular h-BN domains with all N-terminated edges at the first two Cu substrates (position 1 and 2). The higher nucleation density of h-BN on the first piece of Cu is attributed to the dense borazine particles that instigate heterogeneous nucleation, but the amount could

be reduced for the subsequent Cu substrates further away. To further study the growth behavior of h-BN including the orientation dependence and layer number, we focus the analysis on the triangular h-BN grown by OCVD process.

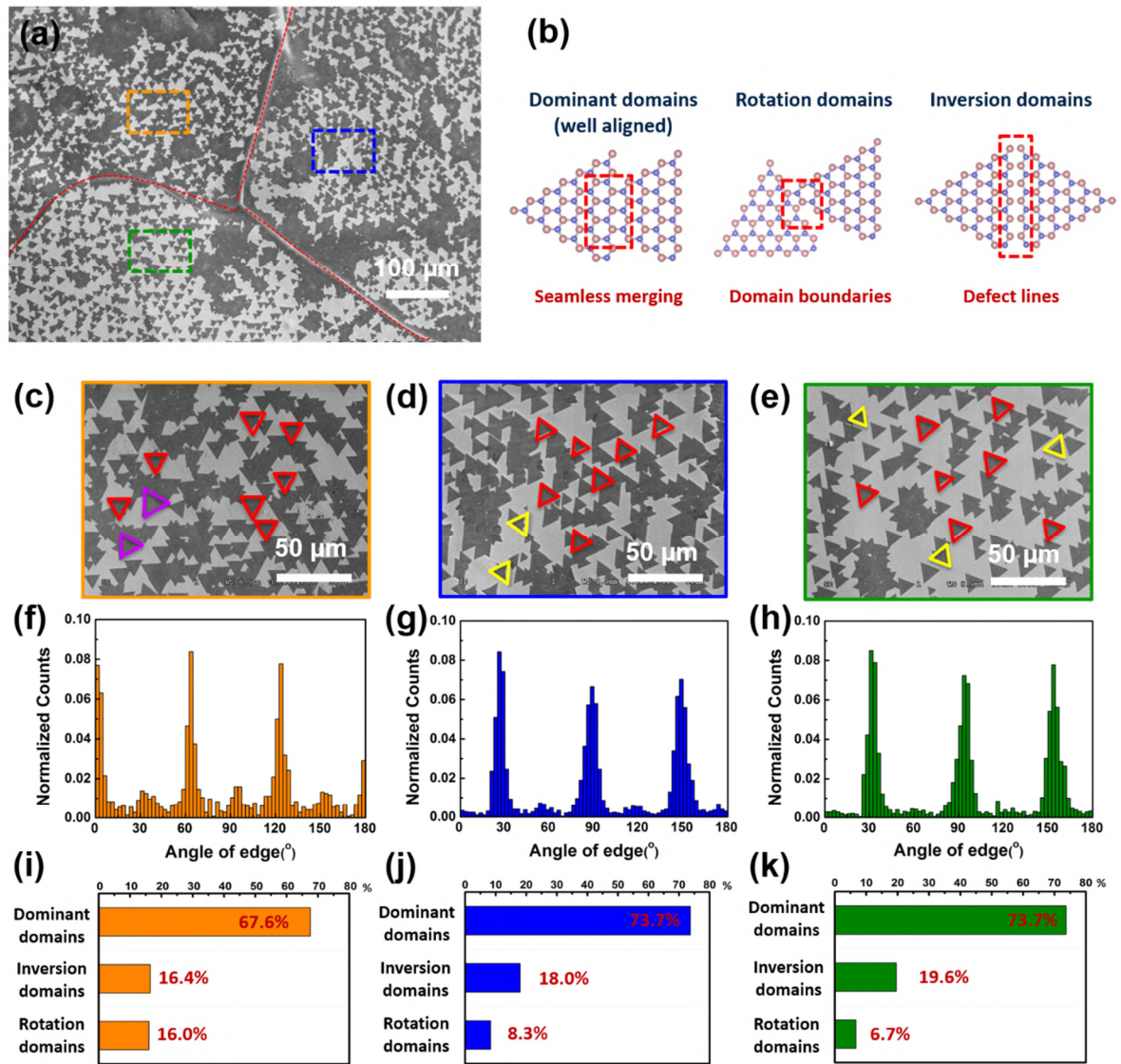


Figure 3. Orientation dependence of triangular h-BN domains grown on Cu. (a) Low-magnification SEM image demonstrating the growth of h-BN crystals on polycrystalline Cu foil by OCVD process with the growth time 40 min. (b) Schematic illustration of atomic configuration for merging between triangular h-BN domains that have different orientation. (c-e) Magnified SEM images chosen from panels selected by different dashed line (orange dashed line for (c), green dashed line for (d) and blue dashed line for (e), respectively) in (a), showing the different preferred growth directions of h-BN triangular domains within each Cu grain. (f-h) Statistical distributions of the edge angles of individual OCVD-grown triangular h-BN domains within each Cu grain shown in (c-e), respectively. (f) Percentage of different type of triangular h-BN domain merging within each Cu grain shown in (c-e), respectively.

Figure 3 displays the orientation dependence of h-BN domains on Cu surface. In the SEM image shown in Figure 3(a), triangular h-BN domains can be observed on three different Cu grains which the grain boundary of Cu is marked by the red dashed line. Closer inspection for each Cu grain marked by the dashed orange, green and blue rectangular is shown in Figure 3(c-e), respectively. The h-BN domains in different Cu grains have preferred growth directions, and the measurement of the edge orientation for each h-BN domain produces histograms of the total number of edges at a given angle. The statistical distributions of the orientations of h-BN triangles in Figure 3(c-e) are shown in Figure 3(f-h), respectively, revealing a propensity of edges separated by 60° from one another. This indicates that most of the dominant triangular h-BN domains within the same Cu grain, as outlined in red, within individual Cu grain are well aligned in the same orientation, indicating an epitaxial relationship between the BN domain and the underlying Cu substrate. Only few of triangular domains are on the different orientations with inversion symmetry or rotation symmetry, as outlined in yellow and purple respectively. Some of the h-BN domains contain additional facets with several 3-fold or 6-fold symmetric orientations forming a variety of complex structures, which may be attributed to the merging of neighboring triangular h-BN domains with the rotation of 30° and 60° when the nucleation sites are closed enough to one another.

The different orientations for h-BN triangles could lead to different types of domain boundaries. As illustrated in Figure 3(b), when two well-orientated triangular domains merge together they could stitch seamlessly and preserve the single-crystalline structure. In comparison, when two misaligned h-BN triangles with different rotation merge together, a domain boundary is formed by pentagon-heptagon pairs or square-octagon pairs. These few misaligned h-BN domains might be attributed to the disturbance arising from the impurities like borazine byproduct on Cu surface or the dislocations on Cu surface generated from the mechanical polishing. When two oppositely orientated domains merge together, a defect line

with B-B or N-N bonding might be generated at the interface. The percentage of these three different orientations of triangular h-BN domains in Figure 3(c-e) are listed in Figure 3(i-k), demonstrating that around 70% of the h-BN triangles are aligned.

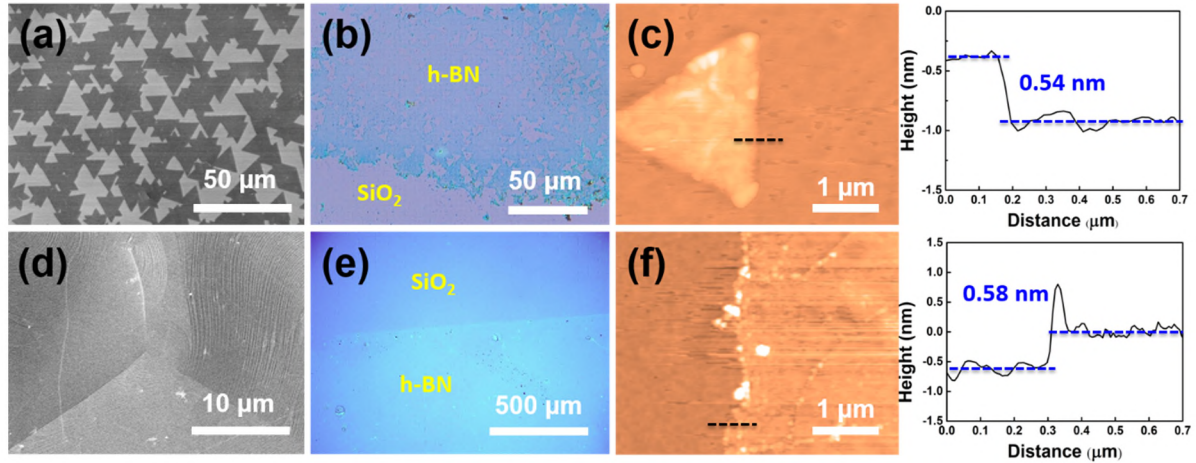


Figure 4. Number of layer characterization for triangular h-BN domain and continuous film grown on Cu by OCVD process. (a) SEM image of triangular h-BN domains grown for 40 min on Cu substrate. (b) Optical image of triangular h-BN domains in (a) transferred to SiO₂/Si substrate. (c) AFM image with the scanned line over the corner of triangular h-BN domain edge. (d) SEM image of continuous h-BN films grown for 60 min on Cu substrate. (e) Optical image of continuous h-BN films in (d) transferred to SiO₂/Si substrate. (f) AFM image with the scanned line over the corner of continuous h-BN film edge.

To further study the characteristics of the OCVD growth h-BN, both the as-grown triangular h-BN domains and continuous h-BN film were transferred to Si substrate with 300 nm oxide layer. The SEM image in Figure 4(a) shows the triangular h-BN domain grown for 40 min on Cu substrate by OCVD process. Increasing the growth time could lead to the continuous h-BN film (Figure 4(d)). It is observed that the wrinkles on the h-BN surface, resulted from the different thermal expansion coefficient between h-BN and Cu during cooling process, were stretched across the Cu grain boundaries, indicating that the h-BN is grown uniformly over the entire Cu substrate surface. Figure 4(b) and 4(e) demonstrate the optical

image of the h-BN domains in Figure 4(a) and h-BN film in Figure 4(d) after the transfer to SiO₂/Si substrate. The optical contrast indicates uniformity and cleanliness of the h-BN surface. Figure 4(c) and 4(f) show the atomic force microscopy (AFM) analysis of the edge for the transferred h-BN domain sample from Figure 4(b) and (e), respectively. The step height for the domain edge is estimated to be about 0.54 nm and 0.58 nm, both consistent to the equivalent thickness of a single-layer in bulk h-BN (~ 0.4 nm). The slightly larger measured value may be attributed to the trapping of the adsorbed molecules (e.g. H₂O) between the h-BN and SiO₂/Si substrate. It is also noted that there are several white dots distributing around the domain edge, which may come from the PMMA residual left on the h-BN surface after transfer process.

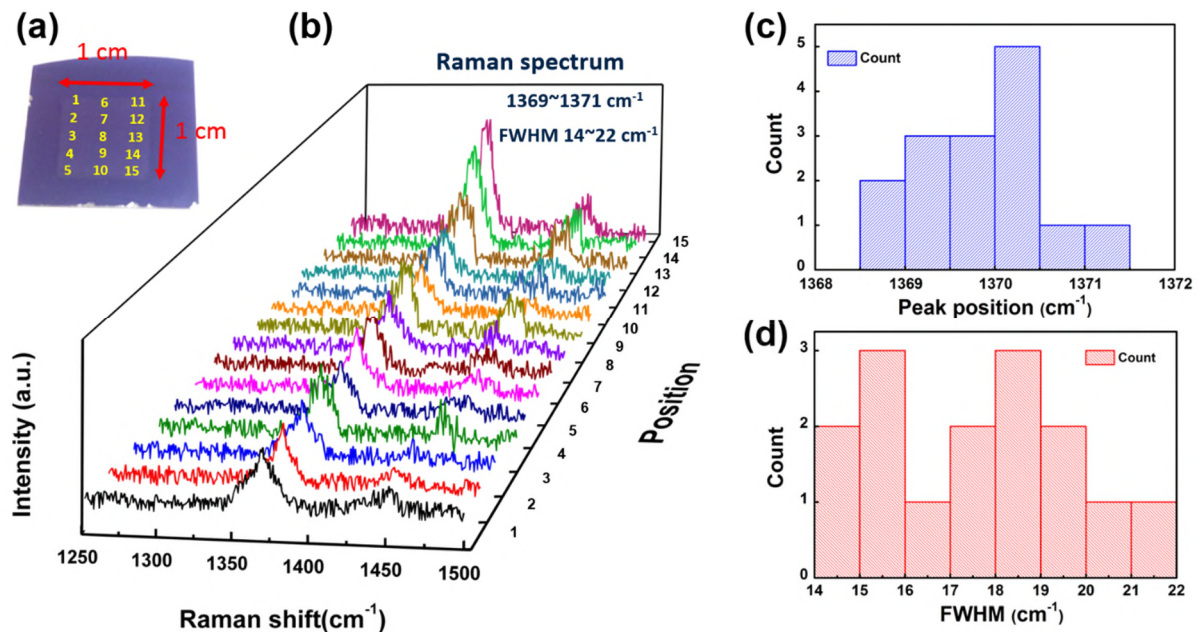


Figure 5. Raman characterization of continuous h-BN film on Si substrate with 300 nm oxide layer. (a) Photograph of 1cm*1cm h-BN film transferred onto SiO₂/Si substrate. (b) Raman spectrum of h-BN on SiO₂/Si substrate at different positions indicated in (a). (c) Histogram for the characteristic peak position of the h-BN film. (d) Histogram for the full width at half maximum (FWHM) of the h-BN film.

To elucidate the uniformity of monolayer h-BN, the OCVD-grown h-BN films were further characterized by Raman spectroscopy. The characteristic peak of h-BN is resulted from the E_{2g} vibration mode and its peak position is related to the layer number. For the bulk h-BN layers, the Raman peak is centered at around 1365 cm^{-1} and shifts to a higher frequency when the layer number is reduced. Figure 5(a) shows the photograph of a continuous h-BN film transferred onto SiO_2/Si substrate. Because the opacity of h-BN layers is nearly zero, the optical contrast of h-BN domains is very weak. The differentiation between monolayer h-BN domains and SiO_2/Si substrate relies on the surface impurities like PMMA residuals from the transfer process left on the film edges. The additional contrast is helpful to distinguish the h-BN boundaries. Figure 5(b) shows the Raman spectra of each position indicated in 5(a) to examine the uniformity of the continuous film. The histogram of the measured E_{2g} peak position and fill width at half maximum (FWHM) are displayed in Figure 5(c) and (d), respectively. Each of Raman peak measured at different position on the h-BN film is located at around $1369\text{-}1371\text{ cm}^{-1}$, with the FWHM ranging from $14\text{-}22\text{ cm}^{-1}$. All of the measured E_{2g} peaks are consistent with previous report on the Raman signature of mechanical exfoliated monolayer h-BN, indicating that the continuous h-BN film has a uniform layer number. It is noted that there is a small peak located around 1450 cm^{-1} in the Raman spectra is caused by the third-order scattering of Si.

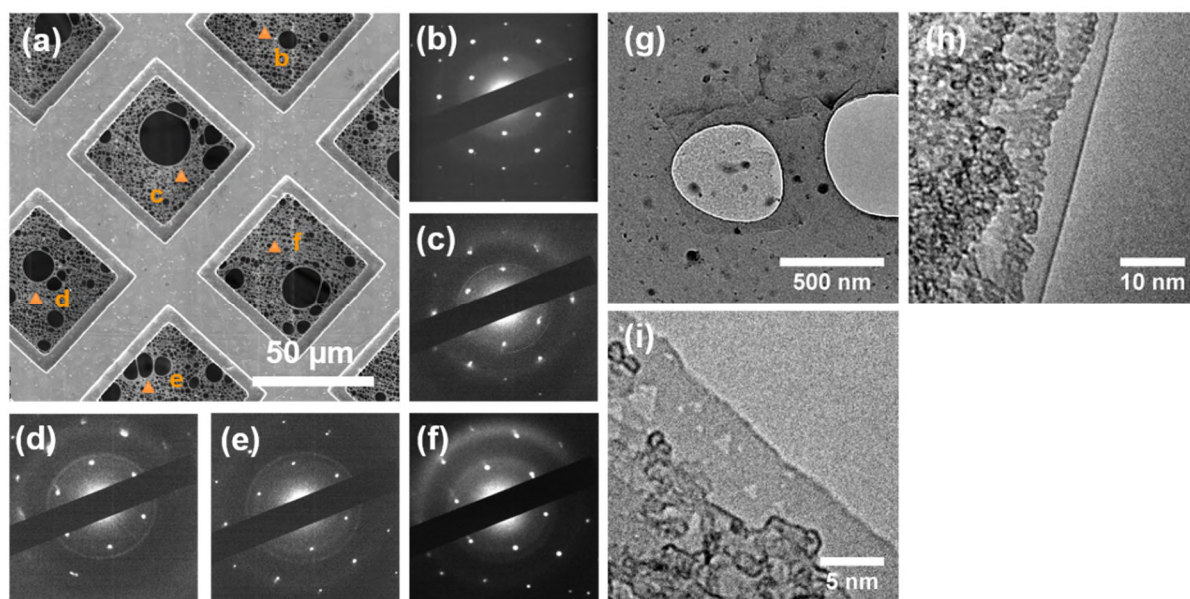


Figure 6. TEM characterization of continuous h-BN films. (a) SEM image of a suspended OCVD grown h-BN film supported on lacey carbon, Cu mesh TEM grid. (b-f) Selected area electron diffraction (SAED) patterns recorded on different location in copper mesh marked in (a). (g) Low-magnification TEM image of an OCVD-grown h-BN. (h-i) High-magnification TEM images of an OCVD-grown h-BN on the folded (h) and open (i) edge, respectively.

The atomic structure of OCVD grown h-BN was further studied by high-resolution (HR) TEM. Figure 5(a) and Figure 5(g) shows the SEM and low-magnification image of h-BN on a lacey carbon coated Cu TEM grid. All the selected area electron diffraction (SAED) patterns, shown in Figure 5(b-f), correspond to locations marked by orange triangles in Figure 5(a) and reveal six-fold symmetric diffraction spots, indicating the high-crystallinity for the as-grown h-BN. The 2D mapping of SAED patterns in Figure 5(a), show single crystal orientations are maintained between locations d, e and f, giving a domain size of about 100 μm, which is much larger than that of an individual triangular h-BN nucleated domain. Locations c and b in figure 5(a) show a rotation of the SAED pattern compared to the lower region and indicate the presence of a grain boundary. Most of the as-grown triangular h-BN domains are well-align in the specific directions as shown in Figure 3(i-k), and could lead to

the seamless stitching when they coalesce into a continuous film. Imaging back-folded edge regions provides a line of contrast to count layer number. There is only one line being observed at the folded edge region (Figure 5(h)), confirming the h-BN grown by OCVD is monolayer. It is also noted that well-orientated triangular holes with various size are observed within the monolayer h-BN region with open edge (Figure 5(i)). These triangular holes were produced from the electron beam irradiation and is in agreement with previous report on TEM imaging of monolayer h-BN films.⁵¹⁻⁵² In addition to the monolayer h-BN, TEM images show small nanoscale regions containing bilayer and multilayer domains, Figure S4(a-b), respectively. Further SEM observation (Figure S4(c)) indicates that the continuous h-BN film is composed of 91.8% monolayer region and 8.2% multilayer region.

Conclusion

In summary, we have demonstrated the significant reduction of nucleation density through the OCVD growth of h-BN, which the formation of passivating oxide layer on Cu surface is preceded by the h-BN growth. The domain size of h-BN can therefore be enhanced from 1 μm to 20 μm and the merger of aligned domains leads to single crystal domains of at least 100 μm . Both AFM and Raman analysis shows that the as-grown h-BN is monolayer with high quality and uniformity. The h-BN grown by OCVD process exhibits strong orientation dependence on the crystallographic orientation of the underlying Cu substrate. Most of the h-BN domains are well-aligned within the same Cu grain, making the grain size of continuous h-BN film possibly equal to that of the grain in the Cu substrate. This work provides a growth route for large crystal domains within h-BN films using Cu rather than expensive Pt film catalysts and opens up further opportunities for CVD grown hBN in devices.

Methods

Synthesis of h-BN by CVD and OCVD process

A piece of 1 cm by 1 cm Cu substrate (Alfa Aesar, 99.8%) with the thickness of 25 μm was first polished by Brasso for at least 15 minutes. The main difference for conventional CVD and OCVD processes is the substrate pretreatment and the heating profile that shown in Figure S1. For conventional CVD growth, the polished Cu substrate was immersed in hydrochloric acid at room temperature for 5 min to remove the native surface oxide, followed by acetone and isopropyl alcohol (IPA) cleaning for 5 min in each step. After loading the Cu substrate, the quartz reactor was flushed with 500 sccm Ar gas for 30 min and then raised to 1000°C under 425 sccm Ar and 75 sccm hydrogen mix gas ($\sim 0.25\%$ hydrogen) flow. The Cu substrate was then annealed at 1000°C for 60 min to remove the residual surface organics and enlarge the grain size of Cu foil. By contrast, during the OCVD growth process the Cu foil was firstly oxidised at 180°C for 5 min in the ambient atmosphere prior to h-BN growth, leading to the formation of thin oxide passivating layer on Cu surface. After loading the Cu substrate, the quartz reactor was flushed with 500 sccm Ar gas for 30 min and then raised to 1000°C under 500 sccm Ar flow and then raised to 1000°C. Both of the conventional CVD and OCVD growth of h-BN were conducted at the atmospheric condition. 8 mg of ammonia borane powder used as a precursor was then heated up in a heating chamber. The h-BN growth was carried out with the typical temperatures for the precursor and the substrate being at about 120°C and 1050°C, respectively, under the 120 sccm hydrogen mix gas flow. After growth, the furnace was slide away from the sample to the other end of the runners, which allow the sample to be fast cooled to room temperature.

Transfer of h-BN

After the cooling process, the as-grown h-BN on the copper foil was firstly coated with a supporting polymer film, polymethylmeth-acrylate (PMMA) at 4500 rpm for 60 seconds. The original copper substrate was then etched in 0.3 M aqueous ammonium persulfate solution. After the copper substrate was removed by etchant solution, the PMMA/h-BN stack was then

floated on DI water three times to eliminate the residual ions from etchant solution. The h-BN layer supported by PMMA was then pasted on to a clean oxidized silicon wafer. After placing the PMMA/h-BN stack on the clean oxidized silicon wafer, the sample was left in the fume hood overnight to slowly evaporate the water trapped between the film and the substrate followed by baked on the hot plate at 180°C for 15 min to enhance the interface contact. Finally, the PMMA supporting layer was removed by placing the sample in acetone for more than 6 hours.

Characterization of h-BN

Scanning electron microscopy (SEM) was performed using a Hitachi-4300 FEG with an accelerating voltage of 3.0 kV. Raman spectroscopy was carried out using a JY Horiba LabRAM Aramis imaging confocal Raman microscope under an excitation wavelength of 532 nm at 12.5mW power focused to a 1 μ m spot size. TEM and SAED was performed using a JEOL 2100 LaB₆ operated at an accelerating voltage of 80kV. Atomic force microscopy (AFM) was performed using an Asylum Research MFP-3D in AC mode with a silicon AC-160TS cantilever (Olympus, spring constant \sim 42 N/m and resonant frequency \sim 300 kHz). Measurements were all done in room-temperature under ambient pressure.

Reference

1. Watanabe, K.; Taniguchi, T.; Kanda, H., Direct-bandgap properties and evidence for ultraviolet lasing of hexagonal boron nitride single crystal. *Nat Mater* **2004**, 3 (6), 404-409.
2. Song, L.; Ci, L.; Lu, H.; Sorokin, P. B.; Jin, C.; Ni, J.; Kvashnin, A. G.; Kvashnin, D. G.; Lou, J.; Yakobson, B. I.; Ajayan, P. M., Large Scale Growth and Characterization of Atomic Hexagonal Boron Nitride Layers. *Nano Letters* **2010**, 10 (8), 3209-3215.
3. Li, L. H.; Cervenka, J.; Watanabe, K.; Taniguchi, T.; Chen, Y., Strong Oxidation Resistance of Atomically Thin Boron Nitride Nanosheets. *ACS Nano* **2014**, 8 (2), 1457-1462.
4. Kho, J.-G.; Moon, K.-T.; Kim, J.-H.; Kim, D.-P., Properties of Boron Nitride (B_xN_y) Films Produced by the Spin-Coating Process of Polyborazine. *Journal of the American Ceramic Society* **2000**, 83 (11), 2681-2683.
5. Tao, O.; Yuanping, C.; Yuee, X.; Kaike, Y.; Zhigang, B.; Jianxin, Z., Thermal transport in hexagonal boron nitride nanoribbons. *Nanotechnology* **2010**, 21 (24), 245701.
6. Liu, Z.; Gong, Y.; Zhou, W.; Ma, L.; Yu, J.; Idrobo, J. C.; Jung, J.; MacDonald, A. H.; Vajtai, R.; Lou, J.; Ajayan, P. M., Ultrathin high-temperature oxidation-resistant coatings of hexagonal boron nitride. *Nature Communications* **2013**, 4, 2541.
7. Kubota, Y.; Watanabe, K.; Tsuda, O.; Taniguchi, T., Deep Ultraviolet Light-Emitting Hexagonal Boron Nitride Synthesized at Atmospheric Pressure. *Science* **2007**, 317 (5840), 932-934.
8. Lee, G.-H.; Cui, X.; Kim, Y. D.; Arefe, G.; Zhang, X.; Lee, C.-H.; Ye, F.; Watanabe, K.; Taniguchi, T.; Kim, P.; Hone, J., Highly Stable, Dual-Gated MoS_2 Transistors Encapsulated by Hexagonal Boron Nitride with Gate-Controllable Contact, Resistance, and Threshold Voltage. *ACS Nano* **2015**, 9 (7), 7019-7026.
9. Britnell, L.; Gorbachev, R. V.; Jalil, R.; Belle, B. D.; Schedin, F.; Katsnelson, M. I.; Eaves, L.; Morozov, S. V.; Mayorov, A. S.; Peres, N. M. R.; Castro Neto, A. H.; Leist, J.; Geim, A. K.; Ponomarenko, L. A.; Novoselov, K. S., Electron Tunneling through Ultrathin Boron Nitride Crystalline Barriers. *Nano Letters* **2012**, 12 (3), 1707-1710.
10. Tran, T. T.; Bray, K.; Ford, M. J.; Toth, M.; Aharonovich, I., Quantum emission from hexagonal boron nitride monolayers. *Nat Nano* **2016**, 11 (1), 37-41.
11. Kim, S. M.; Hsu, A.; Araujo, P. T.; Lee, Y.-H.; Palacios, T.; Dresselhaus, M.; Idrobo, J.-C.; Kim, K. K.; Kong, J., Synthesis of Patched or Stacked Graphene and hBN Flakes: A Route to Hybrid Structure Discovery. *Nano Letters* **2013**, 13 (3), 933-941.
12. Wang, M.; Jang, S. K.; Jang, W.-J.; Kim, M.; Park, S.-Y.; Kim, S.-W.; Kahng, S.-J.; Choi, J.-Y.; Ruoff, R. S.; Song, Y. J.; Lee, S., A Platform for Large-Scale Graphene Electronics – CVD Growth of Single-Layer Graphene on CVD-Grown Hexagonal Boron Nitride. *Advanced Materials* **2013**, 25 (19), 2746-2752.
13. Wang, S.; Wang, X.; Warner, J. H., All Chemical Vapor Deposition Growth of MoS_2 :h-BN Vertical van der Waals Heterostructures. *ACS Nano* **2015**, 9 (5), 5246-5254.
14. Okada, M.; Sawazaki, T.; Watanabe, K.; Taniguchi, T.; Hibino, H.; Shinohara, H.; Kitaura, R., Direct Chemical Vapor Deposition Growth of WS_2 Atomic Layers on Hexagonal Boron Nitride. *ACS Nano* **2014**, 8 (8), 8273-8277.
15. Novoselov, K. S.; Jiang, D.; Schedin, F.; Booth, T. J.; Khotkevich, V. V.; Morozov, S. V.; Geim, A. K., Two-dimensional atomic crystals. *Proceedings of the National Academy of Sciences of the United States of America* **2005**, 102 (30), 10451-10453.
16. Gorbachev, R. V.; Riaz, I.; Nair, R. R.; Jalil, R.; Britnell, L.; Belle, B. D.; Hill, E. W.; Novoselov, K. S.; Watanabe, K.; Taniguchi, T.; Geim, A. K.; Blake, P., Hunting for Monolayer Boron Nitride: Optical and Raman Signatures. *Small* **2011**, 7 (4), 465-468.

17. Coleman, J. N.; Lotya, M.; O'Neill, A.; Bergin, S. D.; King, P. J.; Khan, U.; Young, K.; Gaucher, A.; De, S.; Smith, R. J.; Shvets, I. V.; Arora, S. K.; Stanton, G.; Kim, H.-Y.; Lee, K.; Kim, G. T.; Duesberg, G. S.; Hallam, T.; Boland, J. J.; Wang, J. J.; Donegan, J. F.; Grunlan, J. C.; Moriarty, G.; Shmeliov, A.; Nicholls, R. J.; Perkins, J. M.; Grieveson, E. M.; Theuwissen, K.; McComb, D. W.; Nellist, P. D.; Nicolosi, V., Two-Dimensional Nanosheets Produced by Liquid Exfoliation of Layered Materials. *Science* **2011**, *331* (6017), 568-571.
18. Kim, K. K.; Hsu, A.; Jia, X.; Kim, S. M.; Shi, Y.; Hofmann, M.; Nezich, D.; Rodriguez-Nieva, J. F.; Dresselhaus, M.; Palacios, T.; Kong, J., Synthesis of Monolayer Hexagonal Boron Nitride on Cu Foil Using Chemical Vapor Deposition. *Nano Letters* **2012**, *12* (1), 161-166.
19. Shi, Y.; Hamsen, C.; Jia, X.; Kim, K. K.; Reina, A.; Hofmann, M.; Hsu, A. L.; Zhang, K.; Li, H.; Juang, Z.-Y.; Dresselhaus, M. S.; Li, L.-J.; Kong, J., Synthesis of Few-Layer Hexagonal Boron Nitride Thin Film by Chemical Vapor Deposition. *Nano Letters* **2010**, *10* (10), 4134-4139.
20. Kim, G.; Jang, A. R.; Jeong, H. Y.; Lee, Z.; Kang, D. J.; Shin, H. S., Growth of High-Crystalline, Single-Layer Hexagonal Boron Nitride on Recyclable Platinum Foil. *Nano Letters* **2013**, *13* (4), 1834-1839.
21. Park, J.-H.; Park, J. C.; Yun, S. J.; Kim, H.; Luong, D. H.; Kim, S. M.; Choi, S. H.; Yang, W.; Kong, J.; Kim, K. K.; Lee, Y. H., Large-Area Monolayer Hexagonal Boron Nitride on Pt Foil. *ACS Nano* **2014**, *8* (8), 8520-8528.
22. Kim, S. M.; Hsu, A.; Park, M. H.; Chae, S. H.; Yun, S. J.; Lee, J. S.; Cho, D.-H.; Fang, W.; Lee, C.; Palacios, T.; Dresselhaus, M.; Kim, K. K.; Lee, Y. H.; Kong, J., Synthesis of large-area multilayer hexagonal boron nitride for high material performance. *Nat Commun* **2015**, *6*, 8662.
23. Orofeo, C. M.; Suzuki, S.; Kageshima, H.; Hibino, H., Growth and low-energy electron microscopy characterization of monolayer hexagonal boron nitride on epitaxial cobalt. *Nano Research* **2013**, *6* (5), 335-347.
24. Farwick zum Hagen, F. H.; Zimmermann, D. M.; Silva, C. C.; Schlueter, C.; Atodiresei, N.; Jolie, W.; Martínez-Galera, A. J.; Dombrowski, D.; Schröder, U. A.; Will, M.; Lazić, P.; Caciuc, V.; Blügel, S.; Lee, T.-L.; Michely, T.; Busse, C., Structure and Growth of Hexagonal Boron Nitride on Ir(111). *ACS Nano* **2016**, *10* (12), 11012-11026.
25. Sutter, P.; Lahiri, J.; Albrecht, P.; Sutter, E., Chemical Vapor Deposition and Etching of High-Quality Monolayer Hexagonal Boron Nitride Films. *ACS Nano* **2011**, *5* (9), 7303-7309.
26. Corso, M.; Auwärter, W.; Muntwiler, M.; Tamai, A.; Greber, T.; Osterwalder, J., Boron Nitride Nanomesh. *Science* **2004**, *303* (5655), 217-220.
27. Müller, F.; Grandthyll, S., Monolayer formation of hexagonal boron nitride on Ag(001). *Surface Science* **2013**, *617*, 207-210.
28. Behura, S.; Nguyen, P.; Che, S.; Debbarma, R.; Berry, V., Large-Area, Transfer-Free, Oxide-Assisted Synthesis of Hexagonal Boron Nitride Films and Their Heterostructures with MoS₂ and WS₂. *Journal of the American Chemical Society* **2015**, *137* (40), 13060-13065.
29. Jang, A. R.; Hong, S.; Hyun, C.; Yoon, S. I.; Kim, G.; Jeong, H. Y.; Shin, T. J.; Park, S. O.; Wong, K.; Kwak, S. K.; Park, N.; Yu, K.; Choi, E.; Mishchenko, A.; Withers, F.; Novoselov, K. S.; Lim, H.; Shin, H. S., Wafer-Scale and Wrinkle-Free Epitaxial Growth of Single-Orientated Multilayer Hexagonal Boron Nitride on Sapphire. *Nano Letters* **2016**, *16* (5), 3360-3366.
30. Ismach, A.; Chou, H.; Ferrer, D. A.; Wu, Y.; McDonnell, S.; Floresca, H. C.; Covacevich, A.; Pope, C.; Piner, R.; Kim, M. J.; Wallace, R. M.; Colombo, L.; Ruoff, R. S., Toward the Controlled Synthesis of Hexagonal Boron Nitride Films. *ACS Nano* **2012**, *6* (7), 6378-6385.

31. Jaehyun, H.; Jun-Young, L.; Heemin, K.; Jong-Souk, Y., Synthesis of wafer-scale hexagonal boron nitride monolayers free of aminoborane nanoparticles by chemical vapor deposition. *Nanotechnology* **2014**, *25* (14), 145604.
32. Tay, R. Y.; Li, H.; Tsang, S. H.; Zhu, M.; Loeblein, M.; Jing, L.; Leong, F. N.; Teo, E. H. T., Trimethylamine Borane: A New Single-Source Precursor for Monolayer h-BN Single Crystals and h-BCN Thin Films. *Chemistry of Materials* **2016**, *28* (7), 2180-2190.
33. Sutter, P.; Lahiri, J.; Zahl, P.; Wang, B.; Sutter, E., Scalable Synthesis of Uniform Few-Layer Hexagonal Boron Nitride Dielectric Films. *Nano Letters* **2013**, *13* (1), 276-281.
34. Wang, H.; Zhang, X.; Meng, J.; Yin, Z.; Liu, X.; Zhao, Y.; Zhang, L., Controlled Growth of Few-Layer Hexagonal Boron Nitride on Copper Foils Using Ion Beam Sputtering Deposition. *Small* **2015**, *11* (13), 1542-1547.
35. Glavin, N. R.; Jespersen, M. L.; Check, M. H.; Hu, J.; Hilton, A. M.; Fisher, T. S.; Voevodin, A. A., Synthesis of few-layer, large area hexagonal-boron nitride by pulsed laser deposition. *Thin Solid Films* **2014**, *572*, 245-250.
36. Nakhaie, S.; Wofford, J. M.; Schumann, T.; Jahn, U.; Ramsteiner, M.; Hanke, M.; Lopes, J. M. J.; Riechert, H., Synthesis of atomically thin hexagonal boron nitride films on nickel foils by molecular beam epitaxy. *Applied Physics Letters* **2015**, *106* (21), 213108.
37. Kim, H.; Mattevi, C.; Calvo, M. R.; Oberg, J. C.; Artiglia, L.; Agnoli, S.; Hirjibehedin, C. F.; Chhowalla, M.; Saiz, E., Activation Energy Paths for Graphene Nucleation and Growth on Cu. *ACS Nano* **2012**, *6* (4), 3614-3623.
38. Stehle, Y.; Meyer, H. M.; Unocic, R. R.; Kidder, M.; Polizos, G.; Datskos, P. G.; Jackson, R.; Smirnov, S. N.; Vlassiounk, I. V., Synthesis of Hexagonal Boron Nitride Monolayer: Control of Nucleation and Crystal Morphology. *Chemistry of Materials* **2015**, *27* (23), 8041-8047.
39. Tay, R. Y.; Griep, M. H.; Mallick, G.; Tsang, S. H.; Singh, R. S.; Tumlin, T.; Teo, E. H. T.; Karna, S. P., Growth of Large Single-Crystalline Two-Dimensional Boron Nitride Hexagons on Electropolished Copper. *Nano Letters* **2014**, *14* (2), 839-846.
40. Khan, M. H.; Huang, Z.; Xiao, F.; Casillas, G.; Chen, Z.; Molino, P. J.; Liu, H. K., Synthesis of Large and Few Atomic Layers of Hexagonal Boron Nitride on Melted Copper. *Scientific Reports* **2015**, *5*, 7743.
41. Tay, R. Y.; Park, H. J.; Ryu, G. H.; Tan, D.; Tsang, S. H.; Li, H.; Liu, W.; Teo, E. H. T.; Lee, Z.; Lifshitz, Y.; Ruoff, R. S., Synthesis of aligned symmetrical multifaceted monolayer hexagonal boron nitride single crystals on resolidified copper. *Nanoscale* **2016**, *8* (4), 2434-2444.
42. Song, X.; Gao, J.; Nie, Y.; Gao, T.; Sun, J.; Ma, D.; Li, Q.; Chen, Y.; Jin, C.; Bachmatiuk, A.; Rummeli, M. H.; Ding, F.; Zhang, Y.; Liu, Z., Chemical vapor deposition growth of large-scale hexagonal boron nitride with controllable orientation. *Nano Research* **2015**, *8* (10), 3164-3176.
43. Wu, Q.; Park, J.-H.; Park, S.; Jung, S. J.; Suh, H.; Park, N.; Wongwiriyan, W.; Lee, S.; Lee, Y. H.; Song, Y. J., Single Crystalline Film of Hexagonal Boron Nitride Atomic Monolayer by Controlling Nucleation Seeds and Domains. *Scientific Reports* **2015**, *5*, 16159.
44. Lu, G.; Wu, T.; Yuan, Q.; Wang, H.; Wang, H.; Ding, F.; Xie, X.; Jiang, M., Synthesis of large single-crystal hexagonal boron nitride grains on Cu-Ni alloy. *Nat Commun* **2015**, *6*, 6160.
45. Caneva, S.; Weatherup, R. S.; Bayer, B. C.; Brennan, B.; Spencer, S. J.; Mingard, K.; Cabrero-Vilatelá, A.; Baehtz, C.; Pollard, A. J.; Hofmann, S., Nucleation Control for Large, Single Crystalline Domains of Monolayer Hexagonal Boron Nitride via Si-Doped Fe Catalysts. *Nano Letters* **2015**, *15* (3), 1867-1875.

46. Zhou, H.; Yu, W. J.; Liu, L.; Cheng, R.; Chen, Y.; Huang, X.; Liu, Y.; Wang, Y.; Huang, Y.; Duan, X., Chemical vapour deposition growth of large single crystals of monolayer and bilayer graphene. *Nat Commun* **2013**, *4*, 2096.
47. Hao, Y.; Bharathi, M. S.; Wang, L.; Liu, Y.; Chen, H.; Nie, S.; Wang, X.; Chou, H.; Tan, C.; Fallahazad, B.; Ramanarayan, H.; Magnuson, C. W.; Tutuc, E.; Yakobson, B. I.; McCarty, K. F.; Zhang, Y.-W.; Kim, P.; Hone, J.; Colombo, L.; Ruoff, R. S., The Role of Surface Oxygen in the Growth of Large Single-Crystal Graphene on Copper. *Science* **2013**, *342* (6159), 720-723.
48. Hao, Y.; Wang, L.; Liu, Y.; Chen, H.; Wang, X.; Tan, C.; Nie, S.; Suk, J. W.; Jiang, T.; Liang, T.; Xiao, J.; Ye, W.; Dean, C. R.; Yakobson, B. I.; McCarty, K. F.; Kim, P.; Hone, J.; Colombo, L.; Ruoff, R. S., Oxygen-activated growth and bandgap tunability of large single-crystal bilayer graphene. *Nat Nano* **2016**, *11* (5), 426-431.
49. Chang, R.-J.; Lee, C.-H.; Lee, M.-K.; Chen, C.-W.; Wen, C.-Y., Effects of surface oxidation of Cu substrates on the growth kinetics of graphene by chemical vapor deposition. *Nanoscale* **2017**, *9* (6), 2324-2329.
50. Liu, Y.; Bhowmick, S.; Yakobson, B. I., BN White Graphene with “Colorful” Edges: The Energies and Morphology. *Nano Letters* **2011**, *11* (8), 3113-3116.
51. Jin, C.; Lin, F.; Suenaga, K.; Iijima, S., Fabrication of a Freestanding Boron Nitride Single Layer and Its Defect Assignments. *Physical Review Letters* **2009**, *102* (19), 195505.
52. Warner, J. H.; Rummeli, M. H.; Bachmatiuk, A.; Büchner, B., Atomic Resolution Imaging and Topography of Boron Nitride Sheets Produced by Chemical Exfoliation. *ACS Nano* **2010**, *4* (3), 1299-1304.